nature materials

ARTICLES

PUBLISHED ONLINE: 2 FEBRUARY 2015 | DOI: 10.1038/NMAT4202

Curvature-induced symmetry breaking determines elastic surface patterns

Norbert Stoop[1], Romain Lagrange[1], Denis Terwagne[2†], Pedro M. Reis[2,3] and Jörn Dunkel[1*]

Symmetry-breaking transitions associated with the buckling and folding of curved multilayered surfaces—which are common to a wide range of systems and processes such as embryogenesis, tissue differentiation and structure formation in heterogeneous thin films or on planetary surfaces—have been characterized experimentally. Yet owing to the nonlinearity of the underlying stretching and bending forces, the transitions cannot be reliably predicted by current theoretical models. Here, we report a generalized Swift–Hohenberg theory that describes wrinkling morphology and pattern selection in curved elastic bilayer materials. By testing the theory against experiments on spherically shaped surfaces, we find quantitative agreement with analytical predictions for the critical curves separating labyrinth, hybrid and hexagonal phases. Furthermore, a comparison to earlier experiments suggests that the theory is universally applicable to macroscopic and microscopic systems. Our approach builds on general differential-geometry principles and can thus be extended to arbitrarily shaped surfaces.

Symmetry breaking and structure formation are intrinsically linked. Symmetry-breaking transitions encompass a diverse range of phenomena, from the emergence of large-scale cosmological structures[1] or the formation of sand dunes[2] to crystallization of solids[3] and the development of form and function in living organisms[4,5]. Theoretical analysis of symmetry breaking typically builds on effective nonlinear field equations that describe complex many-particle systems[6] by a few macroscopic field variables. This approach has proved fruitful in identifying generic aspects of structure formation, as exemplified by the Ginzburg–Landau theory of phase transitions[7] and Turing's description of reaction–diffusion patterns[8,9]. Generally, however, it is challenging to derive nonlinear field theories systematically[10–13] from the underlying microscopic dynamics. Instead, effective field equations are often inferred from abstract symmetry considerations and bifurcation theory[14], resulting in a large number of undetermined parameters that limit the predictive power and complicate comparison with experimental data. Here, we systematically derive and experimentally test an effective field theory that predicts quantitatively the surface-pattern selection in curved bilayer systems consisting of a stiff film on a soft substrate (Figs 1 and 2).

Buckling of thin films plays a prominent role in the morphogenesis of multilayered soft tissues, governing the wrinkling of skin[15], fingerprint formation[16] and the development of brain convolutions[17]. In addition to their biological relevance, wrinkling processes under curvature constraints are attracting considerable interest as promising techniques for nanoscale surface patterning[18], microlens array fabrication[19] and adaptive aerodynamic drag control[20]. Recent experiments and simulations suggest that wrinkling patterns may vary strongly with applied stress[21–25] and substrate curvature[20,26–30]. However, so far, the complexity of the numerically implemented tensor equations has prevented a detailed analytical understanding. Despite substantial progress in the theoretical description of planar bilayer membranes[31,32], it is unclear how curvature controls pattern selection in non-planar geometries.

The scalar field theory presented below solves this longstanding problem by providing detailed quantitative predictions for curvature- and stress-induced pattern-formation transitions. Starting from Koiter's shell theory[33], we derive a generalized fourth-order Swift–Hohenberg (GSH) equation for the normal displacement field of a film bound to an arbitrarily curved surface (Supplementary Information). In the case of a spherical geometry, our GSH theory reveals that curvature triggers a transition from labyrinth-like to hexagonal wrinkling patterns through a curvature-induced symmetry breaking in the field equation. The theory further predicts a coexistence region separating two 'pure' phases (Fig. 1a–c). Both the theoretically predicted surface patterns and the analytically predicted phase diagram agree quantitatively with data from our macroscale experiments (Figs 1d–f and 3). The GSH model implies that analogous transitions occur when the compressive stress in the film is increased. This prediction is in agreement with recent microscale experiments[28,34] (Fig. 1g–i), suggesting that the theory is universally applicable to both microscopic and macroscopic systems. As our derivation of the GSH model builds on general differential-geometric principles, it can be extended to arbitrarily shaped surfaces, thus providing a generic framework for future studies of curvature-controlled wrinkling in physical, biological and chemical systems.

Theory of thin-film deformation on soft substrates

Our derivation starts from the covariant Koiter shell equations[33], obtained from three-dimensional elasticity theory through an expansion in the film thickness $h \to 0$ (Fig. 2). Koiter's model expresses the elastic energy of a freestanding curved shell in terms of deformations of its central surface (Supplementary Information). Although the Koiter equations have been successfully used in

[1]Department of Mathematics, Massachusetts Institute of Technology, 77 Massachusetts Avenue, Cambridge, Massachusetts 02139-4307, USA. [2]Department of Civil & Environmental Engineering, Massachusetts Institute of Technology, 77 Massachusetts Avenue, Cambridge, Massachusetts 02139-4307, USA. [3]Department of Mechanical Engineering, Massachusetts Institute of Technology, 77 Massachusetts Avenue, Cambridge, Massachusetts 02139-1713, USA. †Present address: Faculté des Sciences, Université Libre de Bruxelles (ULB), Bruxelles 1050, Belgium.
*e-mail: dunkel@mit.edu

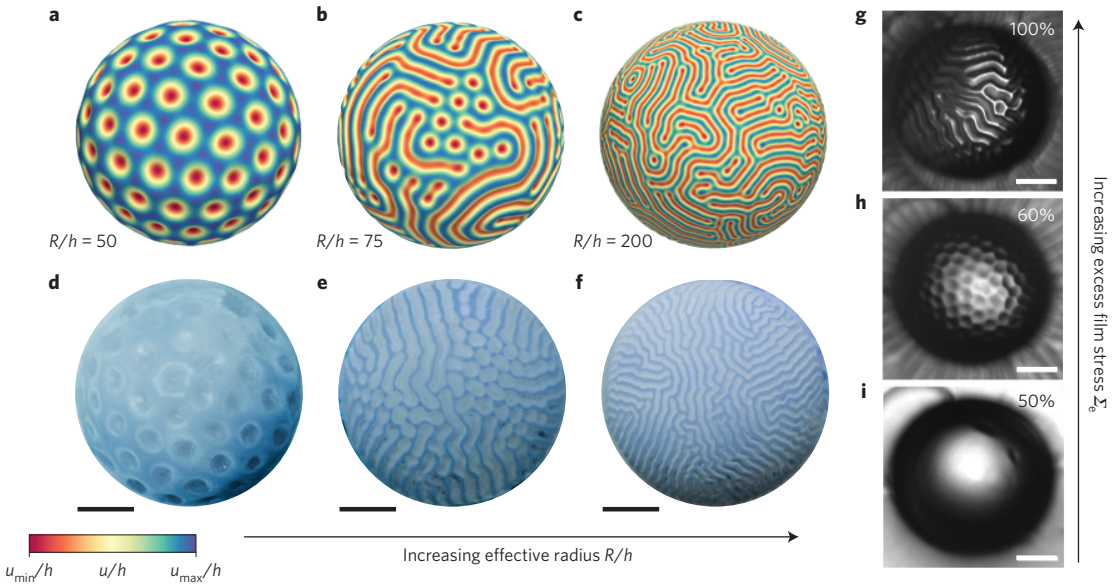

Figure 1 | Macroscopic and microscopic wrinkling morphologies of stiff thin films on spherically curved soft substrates. a–c, Theoretical predictions based on numerical steady-state solutions of equation (1). Colour red (blue) signals inward (outward) wrinkles. Simulation parameters: (**a**) $\gamma_0 = -0.029$, $a = 0.00162$, $c = 0.0025$; (**b**) $\gamma_0 = -0.04$, $a = -1.26 \times 10^{-6}$, $c = 0.002$; (**c**) $\gamma_0 = -0.02$, $a = 1.49 \times 10^{-4}$, $c = 0.0025$ (see Table 1). **d–f**, Experimentally observed patterns confirm the transition from hexagonal (**d**) to labyrinth-like wrinkles (**f**) via a bistable region (**e**) when the radius-to-thickness ratio R/h (see Fig. 2) is increased. Scale bars, 10 mm. Parameters: $E_f = 2{,}100$ kPa, $R = 20$ mm, $\nu = 0.5$ and (**d**) $E_s = 230$ kPa, $h = 0.630$ mm; (**e**) $E_s = 29$ kPa, $h = 0.14$ mm; (**f**) $E_s = 63$ kPa, $h = 0.10$ mm. **g–i**, Oxide layers on microscopic PDMS hemispheres exhibit a similar transition from hexagonal to labyrinth patterns when the excess film stress is increased through changes in the ambient ethanol concentration (indicated in per cent). Scale bars, 250 μm. Micrographs courtesy of D. Breid and A. Crosby[28].

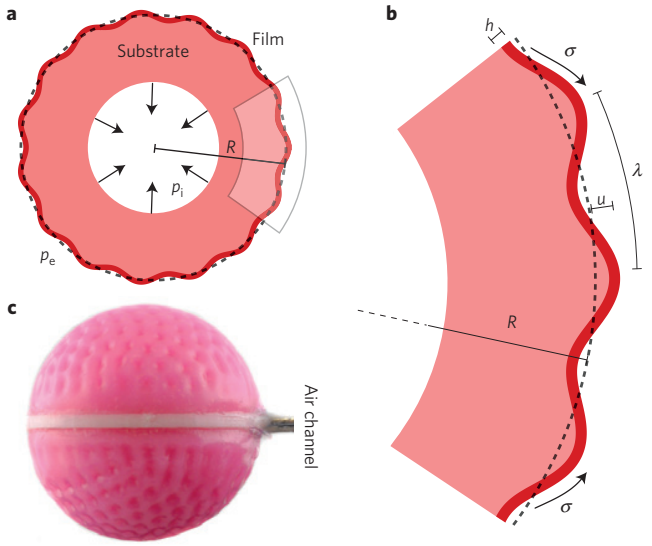

Figure 2 | Notation and experimental system. a, Schematic of a curved thin film adhering to a soft spherical substrate of outer radius R. **b**, The film (thickness h) is driven towards a wrinkling instability by the compressive film stress σ, leading to a wrinkling pattern with wavelength λ and radial displacement u. **c**, The experimental system consists of two merged hemispherical caps. An air channel allows one to tune the film stress σ through the pressure difference $\Delta p = p_e - p_i$.

computational wrinkling studies[26,27], their nonlinear tensorial structure offers limited insight beyond linear stability analysis. We found, however, that substantial analytical simplifications are possible when a stiff film (Young modulus E_f) is adhered to a soft substrate with Young modulus $E_s \ll E_f$.

As relevant to our experiments, which are described in detail below, we consider a spherical geometry with radius $R/h \gg 1$ and assume that film and substrate have the same Poisson ratio ν. The generalization to non-spherical surfaces is obtained by replacing the metric tensor appropriately (Supplementary Information). Continuity across the film–substrate interface favours deformations that are dominated by the radial displacement u (Fig. 2; from here onwards all lengths are normalized by h). Neglecting secondary lateral displacements, one can systematically expand the strain energy, which contains the original Koiter shell energy density as well as additional substrate coupling and overstress contributions, in terms of the covariant surface derivative ∇u and powers of u (Supplementary Information). Functional variation of the elastic energy with respect to u then yields a nonlinear partial differential equation for the wrinkled equilibrium state of the film. Assuming overdamped relaxation dynamics, one thus obtains the following GSH equation (Supplementary Information)

$$\partial_t u = \gamma_0 \Delta u - \gamma_2 \Delta^2 u - au - bu^2 - cu^3 + \Gamma_1 \left[(\nabla u)^2 + 2u\Delta u\right] + \Gamma_2 \left[u(\nabla u)^2 + u^2 \Delta u\right] \qquad (1)$$

Here, Δ denotes the Laplace–Beltrami operator, involving the surface metric tensor of the sphere and Christoffel symbols of the second kind, and Δ^2 is the surface biharmonic operator[35]. The (γ_0, γ_2) terms describe stress and bending, the (a, b, c) terms comprise local film–substrate interactions and stretching contributions, and the (Γ_1, Γ_2) terms account for higher-order stretching forces. For $\Gamma_1 = \Gamma_2 = 0$, equation (1) reduces to the standard Swift–Hohenberg equation, as originally derived in the context of Rayleigh–Bénard convection[10,36]. The additional (Γ_1, Γ_2) terms will prove crucial below when matching theory and experiments. The generalization of equation (1) for arbitrary surfaces is given in Supplementary Equation (34).

The detailed derivation (Supplementary Information), combined with systematic asymptotic analysis of the planar limit $R/h \to \infty$, allows us to express the coefficients in equation (1) in terms of the standard material parameters: Poisson ratio of the film ν,

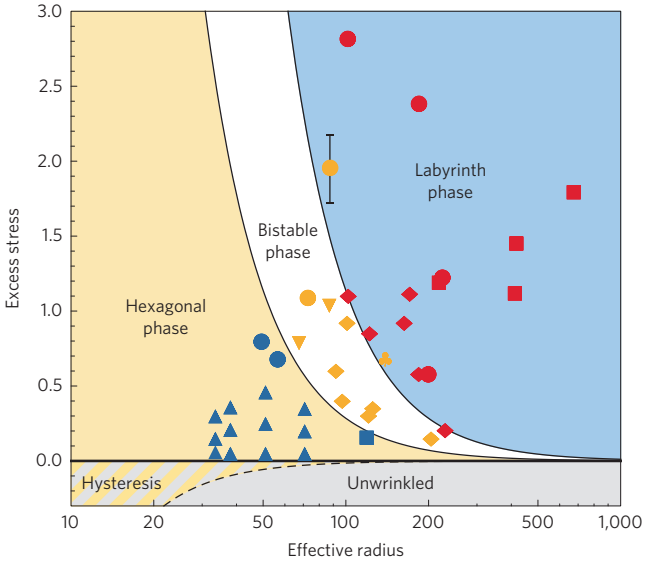

Figure 3 | Phase diagram of wrinkling morphologies. Experimental data points for hexagonal (blue), bistable (yellow) and labyrinth (red) patterns are shown for different values of curvature radius $R/h=\kappa^{-1}$ and excess film stress Σ_e. Symbols indicate the elastic moduli ratio $\eta=3E_s/E_f$ (square, $\eta=0.019$; circle, $\eta=0.036$; clubsuit, $\eta=0.041$; downtriangle, $\eta=0.055$; diamond, $\eta=0.09$; triangle, $\eta=0.328$). The data suggest that phase boundaries are independent of η in the experimentally tested range. Only the largest vertical error bars are shown (standard deviation of 12 amplitude measurements; see Methods). Horizontal error bars are smaller than the symbol size. Solid lines are theoretically predicted phase boundaries, obtained from equation (3) with parameter $c_1=0.0188$ (Table 1).

effective curvature $\kappa=h/R$, Young ratio $\eta=3E_s/E_f$, and excess stress $\Sigma_e=(\sigma/\sigma_c)-1$ (Table 1). The theory contains only a single fitting parameter, c_1, related to the cubic stretching force term cu^3. Equation (1) predicts that the unbuckled solution $u=0$ is stable for negative excess stresses $\Sigma_e<0$, whereas wrinkling occurs for $\Sigma_e\geq 0$. Linear stability analysis at $\Sigma_e=0$ and $\kappa=0$ reproduces the classical[37] pattern-wavelength relation for planar wrinkling, $\lambda/h=2\pi\eta^{-1/3}$ (Supplementary Information).

Numerical simulation of equation (1) is non-trivial owing to the metric dependence of the biharmonic operator Δ^2 (ref. 35). To compute the stationary wrinkling patterns (Fig. 1a–c) predicted by equation (1), we implemented a $\mathcal{C}^1$-continuous finite-element algorithm specifically designed for covariant fourth-order problems (Methods). A main benefit of equation (1), however, is that it enables analytical prediction of the various pattern-formation regimes.

Pattern selection

Pattern selection in the wrinkling regime $\Sigma_e\geq 0$ is a nonlinear process and, therefore, cannot be inferred from linear stability analysis. Numerical parameter scans of equation (1) yield a variety of qualitatively different stationary states that can be classified as representatives of a hexagonal phase (Fig. 1a), labyrinth phase (Fig. 1c) or intermediate coexistence phase (Fig. 1b). Qualitatively, the transition from hexagons to labyrinths can be understood through a symmetry argument: the (b,Γ_1) terms in equation (1) break the radial reflection invariance of its solutions under the transformation $u\rightarrow -u$, as also evident from the corresponding energy functional that is given in Supplementary Equation (37). As b and Γ_1 are controlled by $\kappa=h/R$ (Table 1), we expect a curvature-induced symmetry-breaking transition at some critical value of κ. Furthermore, recalling that the inclusion of similar symmetry-breaking terms causes a transition from labyrinths to hexagonal patterns in the classical Swift–Hohenberg model[36], it is plausible to expect a hexagonal phase at large curvatures κ and labyrinths at smaller values of κ in our system.

Table 1 | List of parameters for equation (1) in units $h=1$, with $\eta=3E_s/E_f$, $\gamma_2=1/12$, $\Sigma_e=(\sigma/\sigma_c)-1$ and $\kappa=h/R$.

$$\gamma_0=-\frac{\eta^{2/3}}{6}-\left[\frac{2(1+\nu)}{\eta^{2/3}}-\frac{1}{3}\right]\kappa^2$$

$$a=\frac{\eta^{4/3}}{12}+\frac{6(1+\nu)-\eta^{2/3}}{3}\kappa^2+\tilde{a}_2\Sigma_e$$

$$b=3(1+\nu)\kappa^3$$

$$c=\frac{2(1+\nu)\eta^{2/3}}{3}c_1$$

$$\Gamma_1=\frac{1+\nu}{2}\kappa$$

$$\Gamma_2=\frac{1+\nu}{2}\kappa^2$$

$$\tilde{a}_2=-\frac{\eta^{4/3}(c+3|\gamma_0|\Gamma_2)}{48\gamma_0^2}$$

The only remaining fitting parameter of the model is c_1.

To obtain a quantitative prediction for the phase boundaries, we approximate equation (1) through a standard Swift–Hohenberg equation and make use of established results from nonlinear stability analysis[38]. Assuming plane-wave solutions with amplitude $\mathcal{A}$ and wavevector k, the Γ_1 term exerts an average force $\Gamma_1\langle(\nabla u)^2+2u\Delta u\rangle_\lambda=-\Gamma_1\mathcal{A}^2k^2/2$ per wavelength λ. One may therefore approximate the Γ_1 term by an effective quadratic force $-\Gamma_1k^2u^2$, and similarly the Γ_2 term by an effective cubic force $\Gamma_2k^2u^3/2$ (Supplementary Information). Inserting for k the most unstable mode, $k_*=\sqrt{|\gamma_0|/(2\gamma_2)}$, equation (1) can be approximated by the standard Swift–Hohenberg equation

$$\partial_t\phi=-2\Delta\phi-\Delta^2\phi-A\phi-B\phi^2-\phi^3 \qquad (2)$$

where $\phi=u/u_*$, $u_*=|\gamma_0|/\sqrt{(c/3)+\Gamma_2|\gamma_0|}$, $A=3a/\gamma_0^2$, and $B=u_*[(b/3)+2|\gamma_0|\Gamma_1]/\gamma_0^2$. Nonlinear stability analysis of equation (2) yields the critical phase transition curves as functions of A and B (ref. 38). Note that the coefficients in equation (2) can be directly traced back to geometric and material parameters, whereas in many other pattern formation processes Swift–Hohenberg-type equations have been applied only in a purely phenomenological manner[6]. In terms of the original system parameters, one finds the stability criteria (Supplementary Information)

$$\begin{aligned}\text{Hexagonal phase:}&\quad -\kappa^2/(20c_1^2)<\Sigma_e<\kappa^2/c_1^2\\ \text{Bistable phase:}&\quad \kappa^2/c_1^2<\Sigma_e<4\kappa^2/c_1^2\\ \text{Labyrinth phase:}&\quad 4\kappa^2/c_1^2<\Sigma_e\end{aligned} \qquad (3)$$

where the parameter c_1 sets the strength of the cubic stretching force (Table 1). In the bistable coexistence phase, both hexagon and labyrinth solutions are stable, suggesting a strong dependence on initial conditions in this regime (Fig. 4).

Equation (3) confirms our qualitative symmetry argument and implies, moreover, that the pattern-formation transitions can be controlled not only by curvature, but also through the excess film stress Σ_e, in agreement with recent experimental results[28] (Fig. 1g–i).

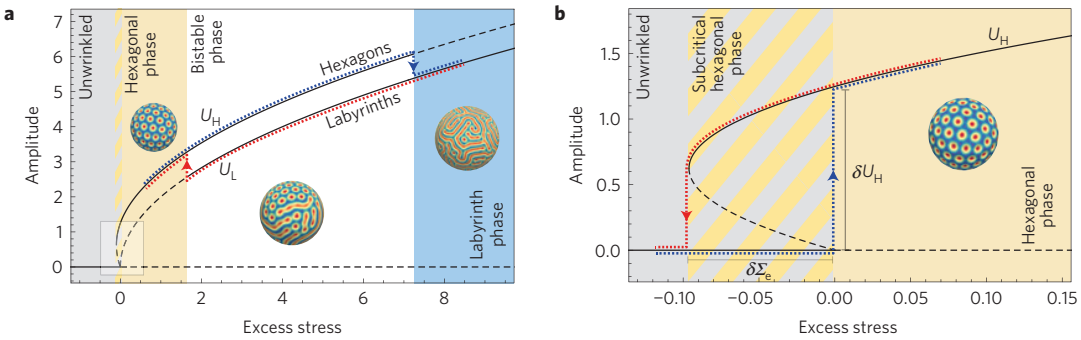

Figure 4 | Bifurcation diagram of wrinkling patterns. Stability analysis of equation (2) predicts two hysteresis cycles, shown here for $R/h = 40$. Solid (dashed) lines correspond to stable (unstable) amplitude solutions; see equation (4) and Supplementary Information. **a**, The hysteresis path across the bistable phase is realized by first decreasing (red) and subsequently increasing (blue) the excess stress Σ_e. **b**, Enlarged view of the second curvature-dependent hysteresis cycle near $\Sigma_e = 0$, corresponding to the highlighted region in **a**. Starting from a stable unwrinkled solution at $\Sigma_e < 0$, the system switches to a hexagonal state at $\Sigma_e = 0$ (blue path). When decreasing the excess stress again to negative values (red), the hexagons remain stable in the subcritical region until a critical value $\Sigma_e = -\delta\Sigma_e$ is reached. The width $\delta\Sigma_e$ and height δU_H of this hysteresis loop depend on curvature $\kappa = h/R$; see equation (4).

Comparison with experiments

We test the theoretical predictions, obtained from equations (1)–(3), by studying the wrinkling of centimetre-sized polydimethylsiloxane (PDMS)-coated elastomer hemispheres (Methods). In our experiments, wrinkling is controlled by the swelling of the film during fabrication and by manual depressurization after fabrication (Fig. 2a,c). The displacement field u, from which the excess film stress Σ_e can be estimated through amplitude measurements[32], is obtained from three-dimensional (3D) surface scans (Methods).

The experimental data confirm quantitatively the theoretically predicted curvature-induced phase transitions from hexagons to labyrinths (Figs 1 and 3). At high values of curvature $\kappa = h/R$, we find the hexagonal phase, characterized by localized spherical depressions that are typically surrounded by 6 neighbours (Fig. 1a,d), although occasional topological defects with 5 or 7 neighbours exist as required by Euler's polyhedral theorem[39]. As predicted by equation (1), experimentally observed hexagons always buckle inwards. For intermediate values of κ, the experiments further confirm coexisting domains of hexagonal and labyrinth-like patterns (Fig. 1b,e). In our simulations of equation (1), we find that the energy of such hybrid patterns remains constant asymptotically, suggesting that they are not transient but correspond to local energy minima. When the curvature is decreased, $\kappa \to 0$, at constant stress Σ_e, the experimental system transitions into the labyrinth phase (Fig. 1c,f), characterized by a network of connected ridges and extended but disconnected valleys (Fig. 1f). Equation (1) shows that this ridge–valley asymmetry is due to the small but non-vanishing symmetry-breaking effect of curvature.

Moreover, in agreement with previous microscale experiments[28] (Fig. 1g–i), equations (1) and (3) imply that the phase transition from hexagons to labyrinths can also be triggered by increasing the excess film stress $\Sigma_e = (\sigma/\sigma_c) - 1$ at constant surface curvature. The morphological phase diagram constructed from our macroscale data confirms this prediction (Fig. 3). In particular, by fixing just a single fitting parameter $c_1 = 0.0188 \pm 0.0002$, the analytical results for the two critical curves in equation (3) are in good quantitative agreement with the experimental data for a wide range of Young modulus ratios $\eta = 3E_s/E_f$ (Fig. 3). Strikingly, we find that the phase boundaries are independent of η over the range $0.019 < \eta < 0.328$ realized in our experiments, suggesting that the parameter c_1 may be a universal numerical constant independent of material properties.

Predictions for future experiments

The good agreement between theory and available experimental data encourages additional predictions that ought to be tested in future experiments. The nonlinear stability analysis of equation (2) suggests that, for sufficiently small overstress Σ_e, the hexagonal phase continues to exist even for weakly curved substrates[32] with $\kappa \ll 1$ (Fig. 3). Simulations of equation (1) for time-varying overstress $\Sigma_e(t)$ confirm that, owing to the presence of symmetry-breaking terms for $\kappa \neq 0$, hexagonal patterns always appear first after crossing the wrinkling threshold $\Sigma_e = 0$ from below. Once the hexagons have been formed, they remain stable throughout the bistable phase when the film stress is slowly increased. A similar reverse effect is observed when the film stress is slowly decreased in simulations that start from the labyrinth phase. In this case, the labyrinths persist throughout the bistable region. Equation (1) makes it possible to understand such memory effects analytically (Fig. 4).

Specifically, the above bifurcation analysis of equations (1)–(3) predicts two hysteresis cycles. The first cycle relates to the onset of wrinkling at $\Sigma_e = 0$ (Fig. 4b), whereas the second encompasses the bistable phase (Fig. 4a). The amplitude $U_H = \max u_H - \min u_H$ of the hexagonal solutions u_H grows according to a square-root law, shifted by the coefficient of the symmetry-breaking term in equation (2) (Supplementary Information),

$$U_H = \frac{3}{5}\left[Bu_* + \sqrt{(Bu_*)^2 + \frac{45\Sigma_e}{4}}\right] \tag{4}$$

where $Bu_* \simeq 3\kappa/(4c_1)$ to leading order in κ, with B and u_* as defined in equation (2). Equation (4) implies that, for $\kappa > 0$, the hexagonal phase is stable subcritically: on reducing the excess film stress from the hexagonal phase, hexagons remain stable even when the film stress is below the critical wrinkling stress σ_c (Fig. 4b). The width of the subcritical region, $\delta\Sigma_e = \kappa^2/(20c_1^2)$, and the amplitude at onset, $\delta U_H = U_H(\Sigma_e = 0) = 9\kappa/(10c_1)$, scale with κ. The bifurcation at $\Sigma_e = 0$ is transcritical, corresponding to a Lifshitz point[38]. Such bifurcations are typical of Swift–Hohenberg-type models, and have been predicted and observed in optics[40] and nonlinear biological and chemical systems[41]. For values of Σ_e in the subcritical hysteresis region, the hexagonal and the flat state are simultaneously stable in a narrow parameter range, potentially allowing for localized hexagonal patterns as found for the standard Swift–Hohenberg equation[42,43].

The detailed analysis of the second hysteresis cycle (Fig. 4a) shows that the amplitude U_L of the labyrinth solutions follows a square-root law (Supplementary Information). Starting from the labyrinth phase, the system remains in a labyrinth state when the film stress is lowered across the bistable region until one reaches the

instability threshold, located at $\Sigma_e \approx 1.75$ in the depicted example with $R/h = 40$ (red path in Fig. 4a). At that point, the system transitions into a hexagonal state. As Σ_e is increased again, the film maintains the hexagonal configuration until the stress exceeds the upper instability threshold $\Sigma_e \approx 7.5$ (blue path in Fig. 4a).

The direct verification of the two predicted hysteresis cycles poses a substantial experimental challenge, requiring high accuracy in the amplitude measurements and precise reversible tuning mechanisms for the excess film stress Σ_e. For instance, the large stress variations needed to trace out the hysteresis loops with a single sample cannot be realized with the present depressurization set-up[20]. Some preliminary experimental support for the hysteresis predictions comes from a recent study[32] of low-stress films, which pointed out the frequent appearance of hexagonal patterns when the excess stress is slowly varied from negative to positive values (see also Fig. 1g–i). These findings are consistent with the results of the above bifurcation analysis (Fig. 4a). We hope that our detailed theoretical predictions will stimulate further experimental work.

In closing, we showed that a systematically derived effective field theory provides a comprehensive quantitative description of surface-pattern formation in non-planar elastic media (see Supplementary Fig. 2 for additional examples with spatially varying curvature). The observation of similar pattern transitions in systems ranging from a few micrometres[26,28,34] to several centimetres[20,27], combined with the fact that curvature-induced pattern selection can now be understood in terms of a symmetry breaking in the effective field equations, suggests that such processes form common universality classes. The generic differential-geometric framework developed here enables a systematic classification of wrinkling phenomena in complex geometries, by examining the symmetry properties of effective higher-order differential operators built from the surface metric and film–substrate coupling forces. Moreover, equation (1) and its generalization to arbitrary shapes (Supplementary Information) provide a basis for studying weakly time-dependent phenomena such as the nucleation of wrinkling patterns under adiabatic (slow) increase of stress. Thus, in practice, the above analytical approach can help us to predict and control wrinkling processes under natural conditions, promising improved microfabrication techniques and, perhaps, even a better understanding of tissue mechanics and developmental morphogenesis.

Methods

Algorithm. The fourth-order covariant derivatives in the metric-dependent biharmonic operator Δ^2 make it challenging to solve equation (1) numerically. We simulate equation (1) by employing an extension of the finite-element scheme, based on subdivision surface basis functions. Previous studies[44,45] show that this method yields high accuracy and excellent performance for related problems in nonlinear elasticity. The underlying algorithm ensures the C^1-continuity of the basis functions, as required for the numerical integration of fourth-order equations. The method also allows for a direct computation of the various covariant derivatives. As in standard finite-element algorithms, we discretize the spherical surface with a mesh consisting of up to 50,000 triangular elements. A solution coefficient u_i is assigned to each of the $i=1,\ldots,N$ triangle vertices, such that the system state is interpolated by $u(\mathbf{r}) = \sum_{i=1}^{N} u_i N_i(\mathbf{r})$, where the N_i terms are the finite-element basis functions. For each time step $[t, t+\Delta t]$, we solve the weak form of equation (1) as a sum over individual element-wise contributions. Starting from random initial conditions with $\|u_i\|^2 < 1-a$, we integrate the dynamics of the system in time using a standard explicit Euler scheme, to obtain the system state $\{u_i\}$ at time $t+\Delta t$. We determine steady-state solutions by continuously monitoring the associated free energy. We consider the system to be in a steady state if its relative change remains below 10^{-5} for more than 10,000 successive time steps.

Experiments. Hemispherical samples were fabricated using rapid digital prototyping techniques that allow flexibility in the choice of geometrical and material parameters[20]. Samples were casted and coated using silicone-based elastomers, such as PDMS (Sylgard 184, Dow Corning), Ecoflex (Smooth-on) and vinylpolysiloxane (VPS, Zhermack), allowing us to examine a wide range of elastic moduli for film (E_f) and substrate (E_s), spanning $9 \le E_f/E_s \le 162$. Typical sample parameters are: outer radius $R = 20$ mm, radius of the inner cavity 9 mm, and film thickness $20\,\mu\text{m} \le h \le 1{,}000\,\mu\text{m}$. The inner cavity of the samples was depressurized to create a state of homogeneous compression and to trigger wrinkling of the stiff surface film. Surface profiles were measured using a NextEngine 3D Laser scanner. The excess film stress Σ_e was estimated from the pattern amplitude $\mathcal{A}$ determined in the 3D surface scans, using the established amplitude versus stress relations $\mathcal{A} = k\sqrt{\Sigma_e}$ from classical wrinkling theory[32], with $k=1$ for labyrinths and $k = 2/\sqrt{11+6\nu-5\nu^2}$ for hexagonal patterns.

Received 17 August 2014; accepted 19 December 2014; published online 2 February 2015

References

1. Bond, J. R., Kofman, L. & Pogosyan, D. How filaments of galaxies are woven into the cosmic web. *Nature* **380,** 603–606 (1996).
2. Parteli, E., Durán, O., Tsoar, H., Schwämmle, V. & Herrmann, H. J. Dune formation under bimodal winds. *Proc. Natl Acad. Sci. USA* **106,** 22085–22089 (2009).
3. Onuki, A. *Phase Transition Dynamics* (Cambridge Univ. Press, 2002).
4. Palmer, A. R. Symmetry breaking and the evolution of development. *Science* **306,** 828–833 (2004).
5. Chirat, R., Moulton, D. E. & Goriely, A. Mechanical basis of morphogenesis and convergent evolution of spiny seashells. *Proc. Natl Acad. Sci. USA* **110,** 6015–6020 (2013).
6. Aranson, I. S. & Tsimring, L. S. Patterns and collective behavior in granular media: Theoretical concepts. *Rev. Mod. Phys.* **78,** 641–692 (2006).
7. Ginzburg, V. L. & Landau, L. D. On the theory of superconductivity. *Zh. Eksp. Teor. Fiz.* **20,** 1064–1082 (1950).
8. Turing, A. M. The chemical basis of morphogenesis. *Phil. Trans. R. Soc. Lond. B* **237,** 37–72 (1952).
9. Ouyang, Q. & Swinney, H. L. Transition from a uniform state to hexagonal and striped Turing patterns. *Nature* **352,** 610–612 (1991).
10. Swift, J. & Hohenberg, P. C. Hydrodynamic fluctuations at the convective instability. *Phys. Rev. A* **15,** 319–328 (1977).
11. Paczuski, M., Kardar, M. & Nelson, D. R. Landau theory of the crumpling transition. *Phys. Rev. Lett.* **60,** 2638–2640 (1988).
12. Delprato, A. M., Samadani, A., Kudrolli, A. & Tsimring, L. S. Swarming ring patterns in bacterial colonies exposed to ultraviolet radiation. *Phys. Rev. Lett.* **87,** 158102 (2001).
13. Brenner, M. P. Chemotactic patterns without chemotaxis. *Proc. Natl Acad. Sci. USA* **107,** 11653–11654 (2010).
14. Wiggins, S. & Golubitsky, M. *Introduction to Applied Nonlinear Dynamical Systems and Chaos* Vol. 2 (Springer-Verlag, 1990).
15. Cerda, E. & Mahadevan, L. Geometry and physics of wrinkling. *Phys. Rev. Lett.* **90,** 074302 (2003).
16. Efimenko, K. *et al.* Nested self-similar wrinkling patterns in skins. *Nature Mater.* **4,** 293–297 (2005).
17. Richman, D. P., Stewart, R. M., Hutchinson, J. W. & Caviness, V. S. Mechanical model of brain convolutional development. *Science* **189,** 18–21 (1975).
18. Bowden, N., Brittain, S., Evans, A. G., Hutchinson, J. W. & Whitesides, G. M. Spontaneous formation of ordered structures in thin films of metals supported on an elastomeric polymer. *Nature* **393,** 146–149 (1998).
19. Chan, E. P. & Crosby, A. J. Fabricating microlens arrays by surface wrinkling. *Adv. Mater.* **18,** 3238–3242 (2006).
20. Terwagne, D., Brojan, M. & Reis, P. M. Smart morphable surfaces for aerodynamic drag control. *Adv. Mater.* **26,** 6608–6611 (2014).
21. Jiang, H. *et al.* Finite deformation mechanics in buckled thin films on compliant supports. *Proc. Natl Acad. Sci. USA* **104,** 15607–15612 (2007).
22. Pocivavsek, L. *et al.* Stress and fold localization in thin elastic membranes. *Science* **320,** 912–916 (2008).
23. Brau, F. *et al.* Multiple-length-scale elastic instability mimics parametric resonance of nonlinear oscillators. *Nature Phys.* **7,** 56–60 (2011).
24. Xu, F., Potier-Ferry, M., Belouettar, S. & Cong, Y. 3d finite element modeling for instabilities in thin films on soft substrates. *Int. J. Solids Struct.* **51,** 3619–3632 (2014).
25. Brau, F., Damman, P., Diamant, H. & Witten, T. A. Wrinkle to fold transition: Influence of the substrate response. *Soft Matter* **9,** 8177–8186 (2013).
26. Cao, G., Chen, X., Li, C., Ji, A. & Cao, Z. Self-assembled triangular and labyrinth buckling patterns of thin films on spherical substrates. *Phys. Rev. Lett.* **100,** 036102 (2008).
27. Li, B., Jia, F., Cao, Y-P., Feng, X-Q. & Gao, H. Surface wrinkling patterns on a core-shell soft sphere. *Phys. Rev. Lett.* **106,** 234301 (2011).
28. Breid, D. & Crosby, A. J. Curvature-controlled wrinkle morphologies. *Soft Matter* **9,** 3624–3630 (2013).
29. Schroll, R. D. *et al.* Capillary deformations of bendable films. *Phys. Rev. Lett.* **111,** 014301 (2013).

30. King, H., Schroll, R. D., Davidovitch, B. & Menon, N. Elastic sheet on a liquid drop reveals wrinkling and crumpling as distinct symmetry-breaking instabilities. *Proc. Natl Acad. Sci. USA* **109,** 9716–9720 (2012).
31. Audoly, B. & Boudaoud, A. Buckling of a thin film bound to a compliant substrate, part i: Formulation, linear stability of cylindrical patterns, secondary bifurcations. *J. Mech. Phys. Solids* **56,** 2401–2421 (2008).
32. Cai, S., Breid, D., Crosby, A. J., Suo, Z. & Hutchinson, J. W. Periodic patterns and energy states of buckled films on compliant substrates. *J. Mech. Phys. Solids* **59,** 1094–1114 (2011).
33. Ciarlet, P. G. *Mathematical Elasticity* Vol. 3 (North Holland, 2000).
34. Yin, J., Han, X., Cao, Y. & Lu, C. Surface wrinkling on polydimethylsiloxane microspheres via wet surface chemical oxidation. *Sci. Rep.* **4,** 5710 (2014).
35. Jost, J. *Riemannian Geometry and Geometric Analysis* (Springer, 2008).
36. Cross, M. C. & Hohenberg, P. C. Pattern formation outside of equilibrium. *Rev. Mod. Phys.* **65,** 851–1112 (1993).
37. Allen, H. G. *Analysis and Design of Structural Sandwich Panels* (Pergamon, 1969).
38. Golovin, A. A. & Nepomnyashchy, A. A. *Self-Assembly, Pattern Formation and Growth Phenomena in Nano-Systems* (Springer, 2006).
39. Coxeter, H. S. M. *Regular Polytopes* (Courier Dover Publications, 1973).
40. Clerc, M. G., Petrossian, A. & Residori, S. Bouncing localized structures in a liquid-crystal light-valve experiment. *Phys. Rev. E* **71,** 015205(R) (2005).
41. Kozyreff, G. & Tlidi, M. Nonvariational real Swift–Hohenberg equation for biological, chemical, and optical systems. *Chaos* **17,** 037103 (2007).
42. Lloyd, D. J. B., Sandstede, B., Avitabile, D. & Champneys, A. R. Localized hexagon patterns of the planar Swift–Hohenberg equation. *SIAM J. Appl. Dyn. Syst.* **7,** 1049–1100 (2008).
43. Burke, J. & Knobloch, E. Localized states in the generalized Swift–Hohenberg equation. *Phys. Rev. E* **73,** 056211 (2006).
44. Cirak, F., Ortiz, M. & Schröder, P. Subdivision surfaces: A new paradigm for thin-shell finite-element analysis. *Int. J. Numer. Methods Eng.* **47,** 2039–2072 (2000).
45. Stoop, N., Wittel, F. K., Amar, M. B., Müller, M. M. & Herrmann, H. J. Self-contact and instabilities in the anisotropic growth of elastic membranes. *Phys. Rev. Lett.* **105,** 068101 (2010).

Acknowledgements

This work was supported by the Swiss National Science Foundation grant No. 148743 (N.S.), by the National Science Foundation, CAREER CMMI-1351449 (P.M.R.) and by an MIT Solomon Buchsbaum Award (J.D.).

Author contributions

N.S., R.L. and J.D. developed the theory. N.S. and R.L. performed analytical calculations. N.S. implemented and performed the numerical simulations. D.T. and P.M.R. developed the experiments. N.S., R.L. and D.T. analysed data. All authors discussed the results and contributed to writing the paper.

Additional information

Supplementary information is available in the online version of the paper. Reprints and permissions information is available online at www.nature.com/reprints. Correspondence and requests for materials should be addressed to J.D.

Competing financial interests

The authors declare no competing financial interests.